

www.acsnano.org

Discovery of Isomerization Intermediates in CdS Magic-Size Clusters

Reilly P. Lynch, Thomas J. Ugras, and Richard D. Robinson*



Cite This: https://doi.org/10.1021/acsnano.4c08319



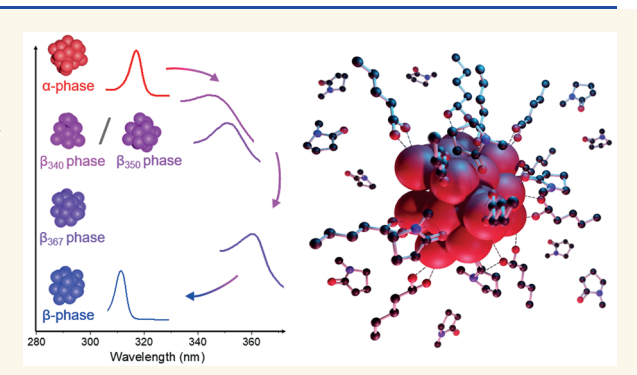
ACCESS

Metrics & More

Article Recommendations

Supporting Information

ABSTRACT: Isomerization, the process by which a molecule is coherently transformed into another molecule with the same molecular formula but a different atomic structure, is an important and well-known phenomenon of organic chemistry, but has only recently been observed for inorganic nanoclusters. Previously, CdS nanoclusters were found to isomerize between two end point structures rapidly and reversibly (the α -phase and β -phase), mediated by hydroxyl groups on the surface. This observation raised many significant structural and pathway questions. One critical question is why no intermediate states were observed during the isomerization; it is not obvious why an atomic cluster should only have two stable end points rather than multiple intermediate arrangements. In this study, we report that the use of amide



functional groups can stabilize intermediate phases during the transformation of CdS magic-size clusters between the α -phase and the β -phase. When treated with amides in organic solvents, the amides not only facilitate the α -phase to β -phase isomerization but also exhibit three distinct excitonic features, which we call the β_{340} -phase, β_{350} -phase, and β_{367} -phase. Based on pair distribution function analysis, these intermediates strongly resemble the β -phase structure but deviate greatly from the α -phase structure. All phases (β_{340} -phase, β_{350} -phase, and β_{367} -phase) have nearly identical structures to the β -phase, with the β_{340} -phase having the largest deviation. Despite these intermediates having similar atomic structures, they have up to a 583 meV difference in band gap compared to the β -phase. Kinetic studies show that the isomers and intermediates follow a traditional progression in the thermodynamic stability of β_{340} -phase/ β_{350} -phase < α -phase < β_{367} -phase < β -phase. The solvent identity and polarity play a crucial role in kinetically arresting these intermediates. Fourier transform infrared spectroscopy and X-ray photoelectron spectroscopy studies paired with simple density functional theory calculations reveal that the likely mechanism is due to the multifunctional nature of the amides that form an amphoteric surface binding bond motif, which promotes a change in the carboxylic acid binding mode. This change from chelating binding modes to bridging binding modes initiates the isomerization. We propose that the carbonyl group is responsible for the direct interaction with the surface, acting as an L-type ligand which then pulls electron density away from the electron-poor nitrogen site, enabling them to interact with the carboxylate ligands and initiate the change in the binding mode. The isomerization of CdS nanoclusters continues to be a topic of interest, giving insight into fundamental nanoscale chemistry and physics.

KEYWORDS: magic-size cluster, isomerization, intermediate, pair distribution function, density functional theory, Stark effect, extreme confinement

INTRODUCTION

Isomerization is a fundamental structural change that occurs in organic molecules, rapidly reorganizing the atomic structure along symmetry-defined pathways.¹ While isomerization in organic molecules has been known for decades, isomerization of inorganic nanoparticles is an emerging area of study that has thus far only been observed in nanoclusters of cadmium sulfide²⁻⁴ and coinage metals⁵⁻¹⁰ as well as studied through computational modeling.¹¹⁻¹³ Though nanocluster isomerization has important fundamental implications for the phase behavior of inorganic nanomaterials, as well as for their surface

chemistry, little is known about the precise underlying mechanism of these transformations. One issue is the limited number of systems and the limited number of structures observed to date. It is perplexing why these phase trans-

Received: June 21, 2024 Revised: August 23, 2024 Accepted: August 23, 2024



formations occur only in select inorganic clusters. For example, InP magic-size clusters do not display isomerism even when similar surface interactions occur. 14,15 More importantly, though, is the lack of information about the transition pathway from the initial to final structure. Intermediate phases are often difficult to study due to their transitory nature, often only existing for femto- to picoseconds. 16 In our previous work, we showed that the use of organic molecules containing hydroxyl functional groups (e.g., alcohols) can facilitate the isomerization of CdS magic-size clusters (MSCs) from the α -phase to the β -phase through hydrogen bonding to surface carboxylates.² This isomerization can be reversed through heating of the β -phase clusters. The transformations were found to be rapid (on the order of picoseconds) with no intermediate states observed, resulting in the conclusion that the transformation is a direct and coherent conversion from one phase to another. This rapid conversion in CdS magic-size clusters has been noted in other reports.⁴ The rapid kinetics of the transformation presents challenges to deciphering whether there are any intermediate states. This gap in knowledge is an important problem; reversible isomerization of inorganic clusters provides an ideal platform to study molecular-like solid-solid transformations and illustrates the important role that surface instabilities can play in directing the equilibrium of atomic structures.

One method to probe this space is to vary the binding strength of the interacting molecule. In the original studies, alcohol and water molecules were used, both of which are very polar. As polarity can be used as a proxy for gauging the amount of excess electron density that can interact with the CdS surface, similar molecules with a lower polarity might be useful to test for intermediate states. Other organic functional groups have been shown to facilitate chemical transformations of CdS MSCs, namely, amines, thiols, and phosphines. Each of these transformed clusters represents a distinct transformation process, leading to separate cluster phases or cluster derivatives. Amides are a good choice due to the resonance delocalization of the electrons between the carbonyl group and nitrogen, leading to a relatively inert molecule with polar groups making them comparable to alcohols.

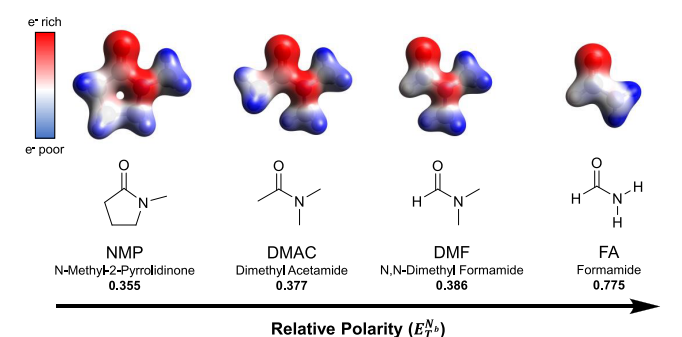
In this study, we use a series of amide molecules to probe the isomerization in CdS MSCs. We find that amides can facilitate the transformation from the α -phase to the β -phase, just like alcohols. Even tertiary amides that are incapable of forming hydrogen bonds are still able to facilitate the isomerization, indicating that hydrogen bonding alone is insufficient to explain the initiation of the isomerization in this case. We also find that due to the distinct interactions of the amides with CdS, the transformations are less aggressive compared to alcohols. Because the amide-induced isomerizations are less rapid, treatment with amides enables the isolation of intermediate states. We study these intermediate phases through X-ray total scattering pair distribution function (PDF) analysis, Fourier transform infrared (FTIR) spectroscopy, X-ray photoelectron spectroscopy (XPS), density functional theory (DFT), and UV-vis absorption spectroscopy to decipher the structural and chemical information of these states. From the structural and optical characterization, we confirm the existence of three intermediate states, which we have named the β_{340} -phase, β_{350} -phase, and β_{367} -phase. All of the intermediates isolated in this study have structures that strongly resemble the previously discovered β -phase. However, despite the nearly identical atomic structure, these

intermediates have band gaps that are redshifted by 325, 439, and 583 meV from the β -phase. These drastically shifted band gaps from the nearly identical inorganic atomic structure indicate a decoupling between the inorganic atomic structure and the electronic band structure. The exact phenomenon driving this decoupling is unclear, but potential explanations include the nanoscale Stark effect 17-19 and extreme confinement.11,12 The apparent decoupling of the electronic states from the inorganic atomic structure in these intermediates enables future investigations on both the underlying mechanism of inorganic isomerizations and the further development of key nanoscale physics. These isolated isomerization intermediates enable structural characterization and represent a paradigm shift in our understanding of inorganic isomerizations. The use of amides to facilitate the isomerization of MSCs shows that the nature of isomerization goes beyond the chemical structure of the initiating species and helps to rationalize why these effects are not seen in larger nanocrystals. The in-solution amide treatment of MSCs enables the observation and isolation of intermediate states during the isomerization process, lending important insight into the underlying mechanism that enables the structural and electronic changes associated with MSC isomerizations. Until this study, no inorganic isomerization intermediate has been isolated or structurally characterized.

RESULTS AND DISCUSSION

Background and Motivation. As previously reported, initially, the CdS MSCs in the α -phase display a strong exciton absorption peak at 324 nm. When solidified films of MSCs are treated with methanol (MeOH) vapor, this peak decreases rapidly and a new peak at 313 nm emerges, indicative of the β -phase, with no evidence of other phases.² In the present study, MSCs were treated with amide species in solution. We chose a series of amides of increasing polarity [N-methyl-2-pyrrolidonne (NMP), dimethyl acetamide (DMAC), N,N-dimethyl formamide (DMF), and formamide (FA)] (Scheme 1) to

Scheme 1. Structures of Amide Species Used to Facilitate MSC Transformations Organized by Increasing Polarity with DFT-Calculated Electron Density Mapped with Electrostatic Potential^a



^aIsosurface values are set to 0.05.

probe the influence that the polarity of the chemical inducing the transformation has on the isomerization process. Along with the polarity of the amides, Scheme 1 also depicts the electron density distributions and electrostatic potentials of each amide as determined through geometry optimization DFT calculations.

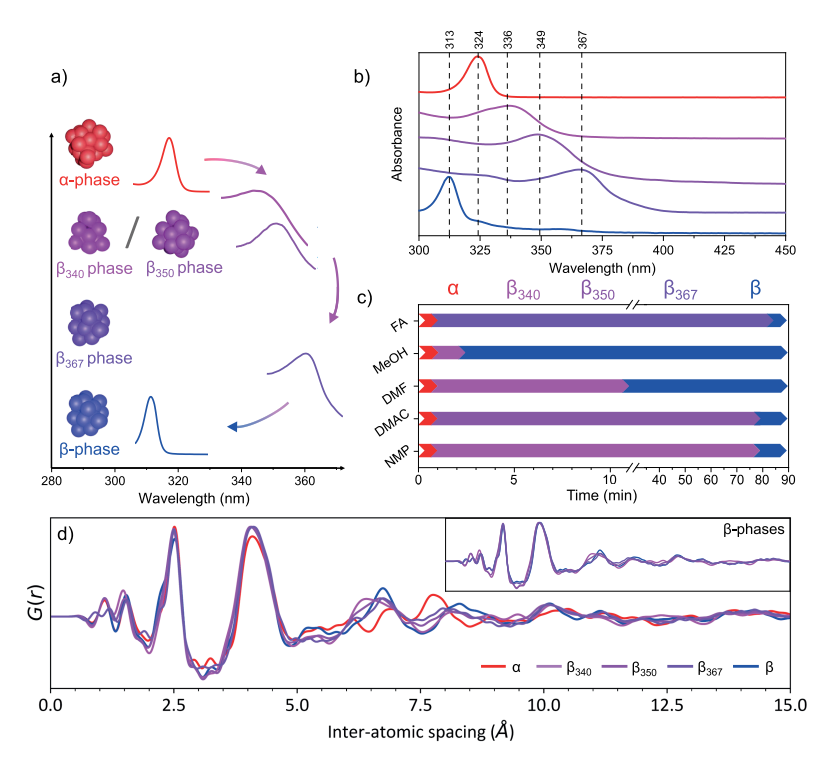


Figure 1. Evidence for intermediate states during the isomerization illustrated through UV—vis absorption spectroscopy and X-ray total scattering with PDF analysis. (a) Diagram showing the transformation from the initial α -phase through three intermediate states and then into the final β -phase, illustrated through colored clusters (left) and shifts in the UV—vis spectra (right). (b) UV—vis spectra of DMAC-treated and DMF-treated MSCs demonstrating the characteristic exciton of the intermediate states. The correlated movement of peaks in the UV—vis absorbance spectrum starts at 324 nm, progresses through up to three redshifts, and concludes with a blueshift to 313 nm. To isolate each isomer, the amide-treated MSC is submerged in various solvent environments, including hexane, chloroform, and THF. (c) Time evolution for the first 90 min of transformation of each amide; arrows represent the progression of the transformation and emergent phase during that time. (d) Overlay comparison of total scattering G(r) plots of each of the five MSC isomer phases. The variations indicate differences in the atomic structure. The three intermediate phases have structures similar to each other and to the final β -phase structure but deviate from the α -phase in the atomic structure beginning around 6 Å. Inset comparison of the β -phases without the α -phase.

Isomerization Pathway and Spectral Decoupling from Atomic Structure. Isomerization Progression. When CdS MSCs are treated with amides, the initial 324 nm exciton absorption peak rapidly decreases in intensity and a welldefined peak centered at 340 or 350 nm emerges (Figure 1a,b). These three peaks are exclusively dependent on the coordinating amide: each amide produces either a 340 or a 350 nm peak but not both (e.g., DMF will only produce a 340 nm peak while DMAC will only produce a 350 nm peak; see Tables S1 and S2). As the transformation progresses, these intermediate peaks diminish as a broad peak at longer wavelengths (~367 nm) appears (Figures 1a,b, S1 and S2). Finally, when the transformation reaches the final β -phase stage, a 313 nm peak is present, and all other features disappear (Figure 1a,b). The overall evolution of the full absorption spectrum through the transitions is exemplified by the treatment of MSCs with DMF and DMAC (Figure 1b). With DMF treatment, the initial MSC 324 nm peak transitions into a stable 340 nm peak, while the DMAC treatment transitions the native peak into a stable 350 nm peak. As will be discussed, samples displaying these intermediate peaks correspond to different phases with crystal structures similar to those of the β -phase. Therefore, we name them based on their UV-vis absorption peak position combined with the β phase structure, resulting in the terms " β_{340} -phase," " β_{350} phase," and " β_{367} -phase." A sequential red and then a blue shift of the exciton peak was previously observed in this system by Yu and Liu in a solution study with alcohol, where the initial peak centered at 323 nm first shifted to 348 nm followed by the evolution of a peak centered at 312 nm. ²⁰ They claimed that their 348 nm intermediate state could not be isolated due to its unstable nature. In our experiment, we are able to stabilize and isolate the intermediates likely due to the manner by which the amides bind to the surface.

The 340 and 350 nm species behave in an identical manner, and both act as the first formed intermediate state and have identical atomic structures (Figure S3), so they will be referred to synonymously while discussing the evolution of the isomerization (hereafter the 'the first intermediate peak' for sake of simplicity). The first intermediate peak is consistently present as a transitory state. The intensity of the first intermediate peak is correlated with the intensity of both the 313 and 324 nm peaks: the first intermediate peak gains intensity at the expense of the 324 nm peak, and the 313 nm peak then gains intensity at the expense of the 350 nm peak (Figure S4). The relationship between these peaks is similar to the pioneering observations by Manna et al., where their CdSe MSCs evolved to larger MSCs and then to nanoparticles, presenting each MSC species as a transitory isolated exciton peak.²¹ Similar behavior has also been observed by Donega et al. in CdTe magic-size nanowires, where peaks evolve as new atomically defined layers grow onto the nanowires increasing their diameter.²² We assign both the 340 and 350 nm peaks to distinct MSC atomic phases and not to an enlargement of the

cluster's size because the first intermediate peak (1) occurs at similar positions for all amide-treated MSCs (either ~340 or \sim 350 nm, Figure S5), (2) does not shift in position for a given amide in a given solvent system, (3) can be the most prominent exciton feature in the spectrum, and these samples with a prominent 340/350 peak can be isolated and stabilized (Figure 1b), (4) the 350 nm species has a secondary exciton feature associated with it (\sim 275 nm) that is not present in the other phases, and (5) reduces in intensity as the final position peak at 313 nm gains in intensity. The 367 nm peak follows the first intermediate and occurs directly before the transformation to the final β -phase and has been observed for every amide species but is absent for MeOH-treated MSCs (Figure S1). The β_{367} -phase has a narrow variance in absorbance features (FWHM = 0.32 eV), and the phase can be isolated. Thus, using amides rather than alcohols enables the isolation of clusters into intermediate phases which are a transition between the initial α -phase and the final β -phase.

Solvent Influence on Transformation. The kinetics of the transformations between phases depends on the amide and the solvent. Figure 1c shows a summary of the temporal duration of the highest intensity peak evolution from the α -phase (324) nm) to the β_{340}/β_{350} -phase, to the β_{367} -phase, and to the final β -phase (313 nm) for reactions run in different solvents. The reactions are run in chloroform to study the evolution of the 350 nm peak and run in hexane for the evolution of the 313 nm peak. The first intermediate peak can persist as the prominent spectral feature for varying durations ranging from 3 to 80 min depending on the type of amide used to treat the MSCs (Figures S6 and S7). The polarity of the solvent used for the transformation influences the time required to transform (Figures 1c and S6-S8). In more polar solvents, the intermediate phases are favored, while in less polar solvents (e.g., hexane), the intermediate phases are not stabilized and the transformation proceeds directly from the α -phase to the β phase (Figure S7), as was reported in our previous solid—vapor studies.² For example, for amide-treated samples in chloroform, the transition to the first intermediate phase proceeds rapidly, the first intermediate phase is then stable on long time scales (weeks), and there is no progression to the β_{367} -phase or β -phase. In contrast, in nonpolar solvents, the transformations to the final β -phase are comparatively rapid. In contrast, in the nonpolar solvent hexane, the amide-treated MSCs evolve directly to the 313 nm peak from the initial 324 nm peak or are inhibited completely due to phase segregation (Figure S7).

There are a few notable exceptions to these trends. FA is the only amide that facilitates a rapid transformation to the β_{367} phase in polar chloroform at room temperature (Figures 1c and S6). In the nonpolar solvent hexane, the intermediatephase 350 nm peak is only observed for DMAC, while all other amides transform directly to the β -phase (Figure S7). The β_{350} phase cannot be isolated in hexane and begins to form the β phase while also coexisting with the remaining α -phase (Figure S7). Most surprising from these results is the finding that MSCs treated with MeOH in solution can present a stable intermediate phase. In chloroform, MeOH-treated samples evolve a peak centered at 350 nm as the major peak (β_{350} phase) and another minor peak at 313 nm (β -phase). The 313 peak then becomes the dominant peak after an extended time (10 min) (Figures S9 and S10, SI Video). This result is surprising because it diverges from our previous findings where MeOH vapor on a solid MSC film caused an immediate transformation to the β -phase without the formation of any intermediate phases.² This result also diverges from solution-phase experiments where a similar direct transformation occurs in hexane when treated with DMF: the DMF treatment directly produces the 313 nm peak (β -phase) from the 324 nm peak (α -phase) within 4 h (see Figure S7). Evidently, solution-phase experiments enable the kinetics and thermodynamics needed to stabilize the intermediate states.

In summary, the intermediate states are much more stable when the MSCs are isomerized with amides and the reaction is run in more polar solvents like chloroform and THF compared to transformations using DMF as the initiator with a solvent of hexanes under identical conditions. We propose that solventscreening effects are key to understanding the effect of the solvent polarity on the transformation mechanism. The transformation is initiated by the interaction with surface ligands. In polar solvents, the isomerization-initiating species interacts with the solvent through the polar groups (i.e., heteroatoms). Because of this selective interaction, the groups on the amide responsible for binding to the surface are screened from interacting with the MSC surface. In contrast, nonpolar solvents like hexane have only alkyl chains, which implies that the primary interaction with the amide would be through dipole-induced dipole interactions. This type of interaction is significantly weaker than dipole-dipole interactions, meaning that in solution, these induced dipoles are comparatively transitory. Meaning that the polar groups on the amide would be less screened and there would be less hindrance of interactions with the MSC surface. This process is analogous to how protic and aprotic solvents influence the nucleophilicity of halides.²³ In nonpolar solvents, the initiating species would be strongly attracted to the charged MSC surface for stabilization with little screening from the solvent, making the transition through the first intermediate phase very rapid. Alternatively, the more polar solvents may establish an equilibrium state where the initiating species are bound to the surface in a transitory manner, cyclically binding to the surface and being resolvated. Nonpolar solvents would be unable to effectively establish this equilibrium because of the poor solubility of the initiating species.

Overview of Differences in Atomic Structure. To determine the correlation in atomic structures, we employed X-ray scattering PDF analysis. PDF analysis uses Bragg and diffuse X-ray scattering to determine the probability of finding the separation of atoms as a function of distance. 24,25 The reduced PDF, G(r), is the Fourier transform of the sample's structure factor and represents the probability of encountering a pair of atoms as a function of distance. G(r) is unique to every atomic structure and thus provides a fingerprint for each individual atomic configuration. Differences in G(r) serve to distinguish structural information. The residual, $R_{\rm w}$, is a quantitative measure of the fit between two PDF data sets (see SI for methods). 26 $R_{\rm w} \leq 0.2$ indicates that the reduced PDF [G(r)] profiles of the two samples match closely meaning their atomic structures are nearly identical (Table 1). 27

Using the reduced PDF plots, we find that the β_{340} -phase and β_{350} -phase samples, the "first intermediate peak" species, represent identical atomic structures, with $R_{\rm w}=0.15$ (Figures 1d and S3). The G(r) of both plots have similar peak positions for the 2.5 Å peak, which corresponds to the first Cd–S bond distance. The next peak position at 4.2 Å, corresponding to the Cd–S–Cd distance, also shows a high correspondence. Deviations start to appear in the series of broad peaks between 6 and 7.5 Å, where the peak intensity of this doublet shifts

Table 1. Summary of $R_{\rm w}$ Comparison Values of the Different Phases

							0.4	
Phase (nm)	313	324	340	350	367	_ 뜻	- 0.4	
313	0	0.38	0.25	0.19	0.13	Bad	- 0.3	-
324	0.38	0	0.41	0.34	0.31		-0.2	₽
340	0.25	0.41	0	0.15	0.28	.=	- 0.2	Valu
350	0.19	0.34	0.15	0	0.20	P P	- 0.1	ē
367	0.13	0.31	0.28	0.20	0	Good I	0.0	

from shorter to longer distances. Comparing the G(r) plots of all β -phases (β_{340} -phase, β_{350} -phase, β_{367} -phase, and β -phase) shows that they all have similar atomic structures, which substantially diverge from the α -phase atomic structure (Figure 1d, inset). All G(r) plots have a nearly consistent structure for interatomic distances up to 6 Å. The peak in the 6–7.5 Å range can be used to distinguish the three beta intermediate structures, with the β_{340} -phase and β_{350} -phase having a much broader peak compared to the β_{367} -phase or β -phase. These clear differences illustrate the distinct atomic structures of several phases, which will be discussed in more depth in a later section. In the following sections, we examine each of these β -phase intermediates individually.

Structural Discussion of the β_{340} **-Phase.** The atomic structure of the β_{340} -phase is distinct from that of the α -phase

but strongly resembles that of the β -phase, as is evident through the PDF plots (Figure 2a-e). There are minor differences in peak position in the G(r) for each of the first three peaks corresponding to the C-C (1.5 Å), Cd-S (2.5 Å), and S-Cd-S (4.0 Å) correlations. There are also significant differences at the higher interatomic spacing including peak shifts and broadening. The Cd-S correlation is shifted (0.03 Å shift) toward a smaller interatomic spacing compared to bulk CdS (Figures 2a and S11). By quantifying the change in the peak position of the Cd-S correlation peak compared to the bulk position, the strain of the MSCs relative to bulk can be determined. The calculated strain in the β_{340} -phase is 1.1%, while the strain in the α -phase is 1.2%. This means that the β_{340} -phase has a strain comparable to the initial MSC strain despite the significnt deviation in atomic structure.

We can amplify and quantify the structural differences between the β_{340} -phase and the α -phase, β_{350} -phase, β_{367} -phase, and β -phase by plotting the reduced PDF difference function, $\Delta G(r)$. $\Delta G(r)$ is defined as the difference between two reduced PDFs: $\Delta G(r) = G(r)_1 - G(r)_2$. Comparing the β_{340} -phase to the α -phase, $\Delta G(r)$ has significant amplitude across the interatomic range up to 10 Å (Figure 2b). $\Delta G(r)$ comparing the β_{340} -phase to the β_{350} -phase shows low amplitude suggesting negligible differences in the atomic structure of these isomers (Figure 2c). The amplitude for

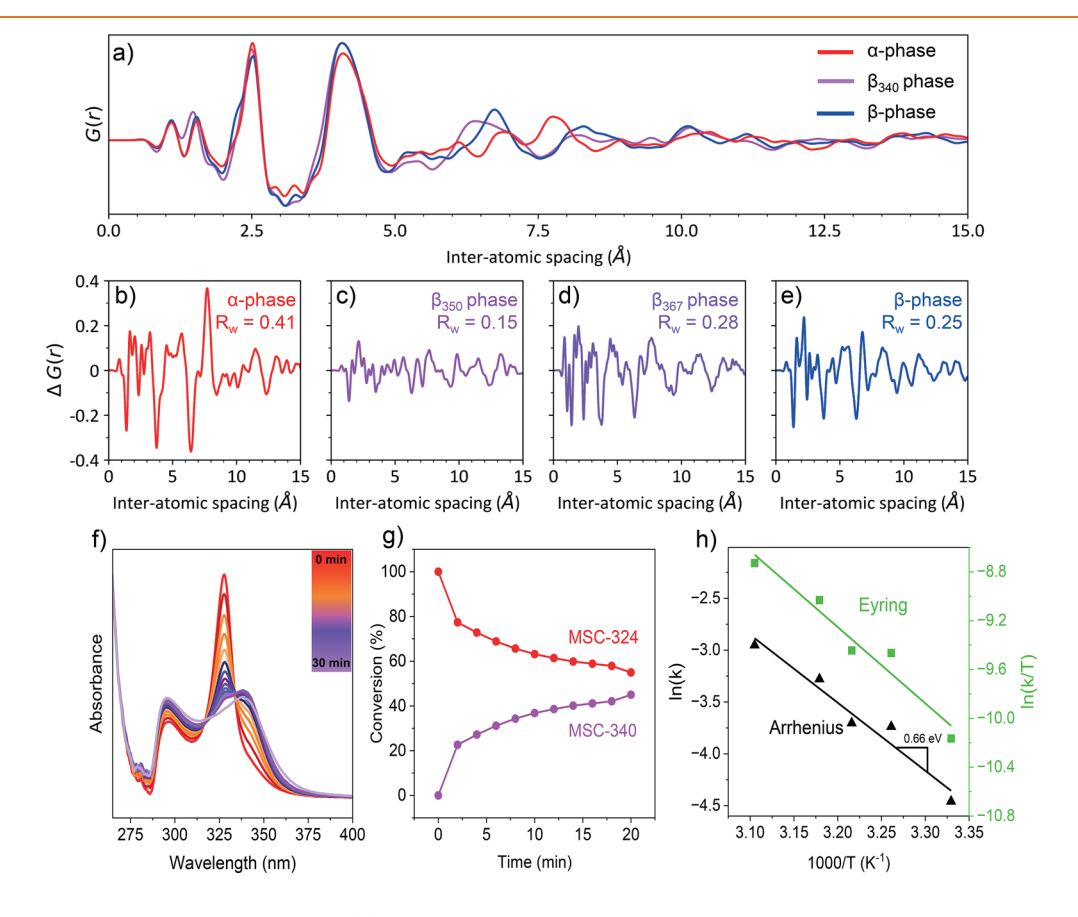


Figure 2. Structure and kinetics of the β_{340} -phase. (a) Reduced PDF of MSCs in the β_{340} -phase compared to the initial α -phase (324 nm) and final β -phase (313 nm). Reduced PDF difference function, $\Delta G(r)$, of the β_{340} -phase compared to the (b) α -phase, (c) β_{350} -phase, (d) β_{367} -phase, and (e) β -phase. $R_{\rm w}$ values quantify the differences between the two atomic structures. (f) Time-resolved UV-vis spectra of DMF-treated MSCs in THF showing the evolution of the peak centered at 340 following the reduction in the peak centered at 324 nm over the course of 30 min. (g) Conversion data based on the evolution of the β_{340} -phase peak. The α -phase data level off at 50% conversion due to poor peak resolution. (h) Kinetic study showing the Arrhenius plot (black) indicating an activation energy of 0.66 eV and the Eyring plot (green) indicating the transformation kinetics are dominated by enthalpic forces.

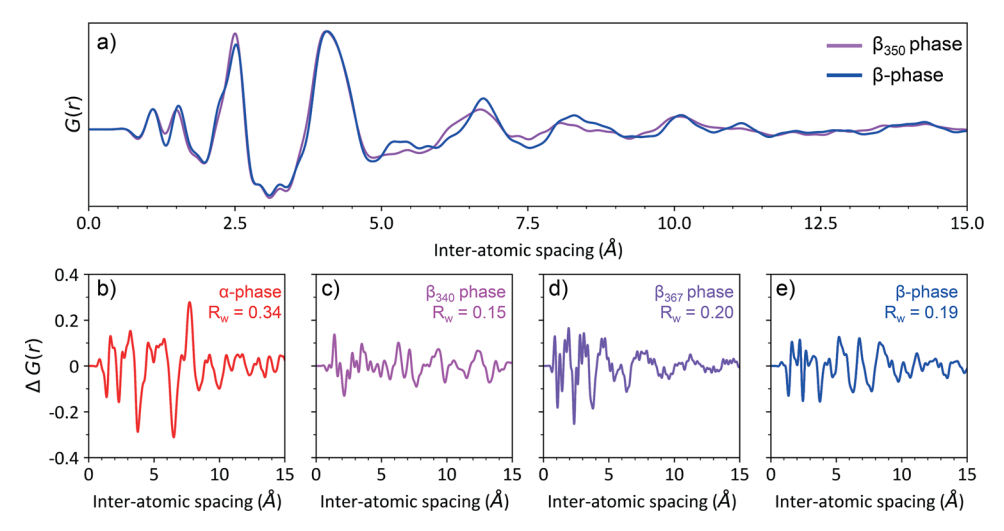


Figure 3. Structural investigation of the β_{350} -phase. (a) Overlay comparison between the β_{350} -phase and the β -phase. $\Delta G(r)$ of the β_{350} -phase compared to the (b) α -phase, (c) β_{340} -phase, (d) β_{367} -phase, and (e) β -phase. $R_{\rm w}$ values quantify the differences between isomer atomic structures. The atomic structure of the β_{350} -phase closely resembles the β_{350} -phase, β_{367} -phase, and β -phase.

 $\Delta G(r)$ compared to the β_{367} -phase and β -phase has low intensity peaks at similar distances and indicates minor differences (Figure 2d,e). The $R_{\rm w}$ values for the reduced PDF of the β_{340} -phase compared to the initial (α -phase) and MeOH (β -phase) samples are 0.42 and 0.27, respectively, clearly showing that the β_{340} -phase has a distinct atomic structure, different from both the α -phase and β -phase but bearing a stronger resemblance to the β -phase (Figure 2b,e inset). The $R_{\rm w}$ values for the β_{340} -phase compared to the β_{350} -phase indicate that these phases are nearly indistinguishable structurally, while the β_{340} -phase compared to the β_{367} -phase and to the β -phase has a similar structure, but $R_{\rm w}$ values that correspond to poor structural overlap (Figure 2c,d inset). All of these metrics indicate that the β_{340} -phase is a structurally distinct intermediate state, correlating to only the β_{350} -phase.

To investigate the thermodynamics and kinetics of this intermediate isomerization, time studies probing the conversion and rate laws governing the transformation were performed using time-resolved UV-vis spectroscopy (Figure 2f-h). Because absorbance is proportional to concentration through the Beer-Lambert law, the two can be treated as equivalent through comparison. ²⁹ A redshift in the UV-vis absorption spectrum with the emergence of a broadening shoulder centered at 340 nm is observed after DMF is added in situ, and the transformation is complete within 30 min (Figure 2f). Conversion data from the 324 species to the 340 species based on the area under the curve of Gaussian fits were also studied (Figure S12). (Note that toward the end of the study, the two peaks are very poorly resolved from each other, so the analysis is ceased at this point and the conversion curves level off.) The MSC-340 signal begins to asymptotically approach 50% conversion at around 15 min as does the MSC-324 signal (Figure 2g). The asymptotic behavior is attributed to the peak broadening of the MSC-340 peak. These conversion data were fit independently, showing that the 340 state is populated as the 324 state is depopulated.

Kinetics studies indicate that the transformation follows firstorder kinetics. The Arrhenius plot is the logarithm of the reaction rate constant plotted against the inverse temperature; the slope of the plot represents the activation energy of the reaction. The Eyring plot assumes a constant enthalpy and

entropy of activation, and the slope can be used to determine whether the process is driven enthalpically or entropically (see SI for methods). From the Arrhenius plot, an activation energy of 0.66 eV was calculated (Figure 2h). The activation energy is 0.33 eV lower than previously reported for the forward (324 to 313 nm) MeOH transformation of solid CdS MSC films.² Several factors in this study might explain the differences between these values, such as the state of matter (solution vs solid film), the initiating species, and the final state of the transformation. The Eyring plot was used to calculate a negative difference in the entropy ($\Delta S = -2.9 \text{ meV}$) and a positive enthalpy ($\Delta H = +0.53$ meV), indicating that the reaction is enthalpically driven (Figure 2h) and also implying that the β_{340} -phase is less thermodynamically stable (higher energy) than the native α -phase MSCs. Previous kinetics studies probing the direct transformation from the α -phase to β -phase found that the β -phase is more thermodynamically stable than the α -phase.² Based on these kinetic data, the thermodynamic stability of the MSC isomers is as follows: β_{340}/β_{350} -phase < α -phase < β_{367} -phase < β -phases, meaning that the intermediate MSCs are metastable compared to the end-state isomers and can only be accessed as a kinetic

Structural Discussion of the β_{350} -Phase. By examining the reduced PDF [G(r)] plots, we find that the β_{350} -phase has a nearly identical atomic structure to the β -phase (Figure 3a). The reduced PDF difference function, $\Delta G(r)$, shows significant differences between the eta_{350} -phase and the lphaphase through large amplitudes in $\Delta G(r)$ up to 10 Å (Figure 3b). Interestingly, the β_{350} -phase shows less differences compared to the β_{367} -phase and β -phase and is nearly indistinguishable from the β_{340} -phase (Figure 3c–e). The $R_{\rm w}$ comparison is larger than 0.2 for the α -phase and the β_{367} phase (Figure 3b-e, inset). The most significant differences between the β_{340} -phase and the β_{350} -phase are the peaks around 6.6 Å. Through the progression of the transformation, the peak positions both gradually focus to the β -phase peak positions illustrating the rearrangement of atoms into the β phase through the intermediates (Figure S13). Interestingly, the β_{340} -phase and β_{350} -phase seems to overshoot the position of the β -phase positions, then correct through the β_{367} -phase.

Since this correlation belongs to the surface-to-core distance, it implies that the MSC first contracts then relaxes into the final β -phase, though the β -phase is still significantly compressed compared to the α -phase.

Impact of Amide Identity on the Atomic Structure of the β_{367} -Phase. In comparison to the other intermediates, the β_{367} -phase, despite exhibiting a drastically shifted excitonic feature, strongly correlates with the atomic structure of the β phase. This contrasts with the β_{340} -phase, which has a distinct atomic structure from the β -phase, and parallels the β_{350} -phase, which is very similar to the β -phase. Unlike the other phases, the β_{367} -phase can be accessed by every amide, making it the ideal species to study the influence the amide identity has on the atomic structure. By overlaying the G(r) of the amidetreated, β_{367} -phase MSCs, the differences between the functions become apparent (Figure 4, see SI for methods). Comparing the β_{367} -phase MSCs to the initial α -phase MSCs, the peak profiles at distances shorter than 5 Å look identical with only minor variations (Figure 4a, top). However, at distances greater than 5 Å, there are major discrepancies. The most significant difference is associated with the peak centered at 7.7 Å, which correlates with a surface-core distance (about four bonds). In the amide-treated samples, this peak is shifted to longer interatomic spacings and decreases in intensity, suggesting that the bond angle is changing within the tetrahedral coordination environment. Interestingly, a minor peak in the α -phase centered at 6.9 Å increases in intensity and shifts toward smaller interatomic spacings for the amidetreated MSCs. This trend indicates that the second Cd-S correlation distance is shortening, which means that the average distance between Cd and S ions that are not directly bonded together is decreasing, indicating long-range structural changes. Examining the $\Delta G(r)$ comparisons to the α -phase (Figure 4a, bottom) reveals that there are differences between the structures at certain interatomic spacings. There are four peaks in the $\Delta G(r)$ centered at 2.42 Å, corresponding to the first Cd-S correlation, 3.63 Å, corresponding to a peak shoulder at shorter interatomic spacings associated with the first Cd-S-Cd correlation, 5.61 Å, corresponding to the shift of 6.9 Å peak which may be associated with the second Cd-S correlation, and 7.70 Å, corresponding to the surface-to-core distance of the inorganic core (Figure 4a).

On the other hand, comparing G(r) plots between the amide-treated β_{367} -phase MSCs and the MeOH-treated β phase MSCs reveals only minor differences (Figure 4b, top), and the $\Delta G(r)$ comparison also shows very little variation (Figure 4b, bottom). In the region below 5 Å, there are minor differences that do not appear to correlate to any given atomic pair spacing peak, suggesting that the $\Delta G(r)$ is from background noise. There are two interatomic spacings in the $\Delta G(r)$ compared to MeOH that show substantial differences centered at 6.62 and 8.39 Å which are tertiary and quinary correlations, respectively. These differences indicate that the β_{367} -phase and β -phase differ from each other in terms of bond angle, but they maintain similar Cd-S bond lengths. Overall, the intensity of the peaks in the $\Delta G(r)$ of the β_{367}/β -phase comparison is lower than in the $\Delta G(r)$ of the β_{367}/α -phase comparison by more than 40%. The low $\Delta G(r)$ of the β_{367}/β phase comparison confirms that the atomic structures of the amide-treated MSCs are similar to those of the β -phase (Figure 4b).

Each of the amide-treated MSCs in the β_{367} -phase were compared to the initial G(r) and MeOH G(r) through their

residual function (R_w) values²⁸ (Figure 4c, R_w for comparison to α -phase in red, axis at left, $R_{\rm w}$ for comparison to β -phase in blue, axis at right) (see SI for methods). The R_w value determines the fit with an $R_{\rm w} \leq 0.2$, indicating a good structural fit. The first points on the plot (Figure 4c, leftmost points) compare the α -phase to itself and to the β -phase. As expected, $R_{\rm w}$ = 0, indicating a perfect fit for the α -phase compared to itself (Figure 4c, leftmost red point), while the comparison to the β -phase is 0.375, indicating substantial differences in the atomic structure. These fits, however, invert for the amide-treated MSCs. All amide β_{367} -phase MSCs show a strong correlation with the β -phase with all $R_{\rm w}$ values ≤ 0.2 . As arranged from less to more polar, left to right on the plot in Figure 4c, we generally find a trend following the polarity of the amide species. The more polar the amide, the closer the MSCs resemble the atomic structure of the MeOH β -phase and the less they resemble the initial α -phase atomic structure, except for FA which still has a match to the β -phase but not as strongly as the next nearest polar molecule of MeOH (Figure

Interestingly, the species which were isolated in the β_{367} phase all have an $R_{\rm w}$ value of less than 0.2, meaning that despite the 583 meV difference in the excitonic absorption peak position, the β_{367} -phase and the β -phase have nearly identical atomic structures. The discrepancy between the atomic and electronic structures could be a result of surface charging from the binding of the amides to the surface. The surface charging may induce absorbance shifts through the Stark effect which has been shown to cause shifts in the emission spectra of QDs. Owen et al. showed that treatment of CdS and CdSe nanocrystals with amine ligands and metal precursors dramatically increased the PLQY of the crystals but also caused a small redshift (3.7 meV) in the absorbance spectrum.³⁰ The redshift was attributed to either changes in the dielectric environment or changes in the confining potential at the surface. The shift they reported is 2 orders of magnitude too low to fully account for the large redshift observed in our amide-treated samples. However, another study by Sardar et al. showed that a similar treatment of CdSe clusters causes significant redshifting (237.6 meV) in the absorbance spectrum.³¹ Further, their peak broadened significantly, which closely matches the behavior of the β_{340} phase (Figure 2f). This change in the exciton profile was attributed to the delocalization of confined exciton wave functions into the interfacial electron states of the interaction between the LUMOs of the nanocrystal and cadmium complex ligands. Other ligand engineering related shifts in excitonic spectra have also been observed for CdSe MSCs (65.3 meV).³² A confinement-related hypothesis for a spectral shift from CdS MSC isomerization was explored by Mulvaney and co-workers using several different types of molecules (i.e., alcohols, thiols, amines, and phosphines).11 They posit that the shift in absorbance features arises from MSCs existing in an extreme confinement regime. The confinement makes the overlap of MSC wave functions and the wave functions of the initiating molecular species more facile, leading to modification of the band structure and resulting in changes in absorption features rather than a decrease in quantum confinement (α -phase to β phase = 134.6 meV). This overlap of molecule-MSC wave functions explains why significant changes in optical properties are not observed for larger nanocrystals and bulk materials. 12 Interestingly, InP MSCs do not display modifications to their

ACS Nano www.acsnano.org Article

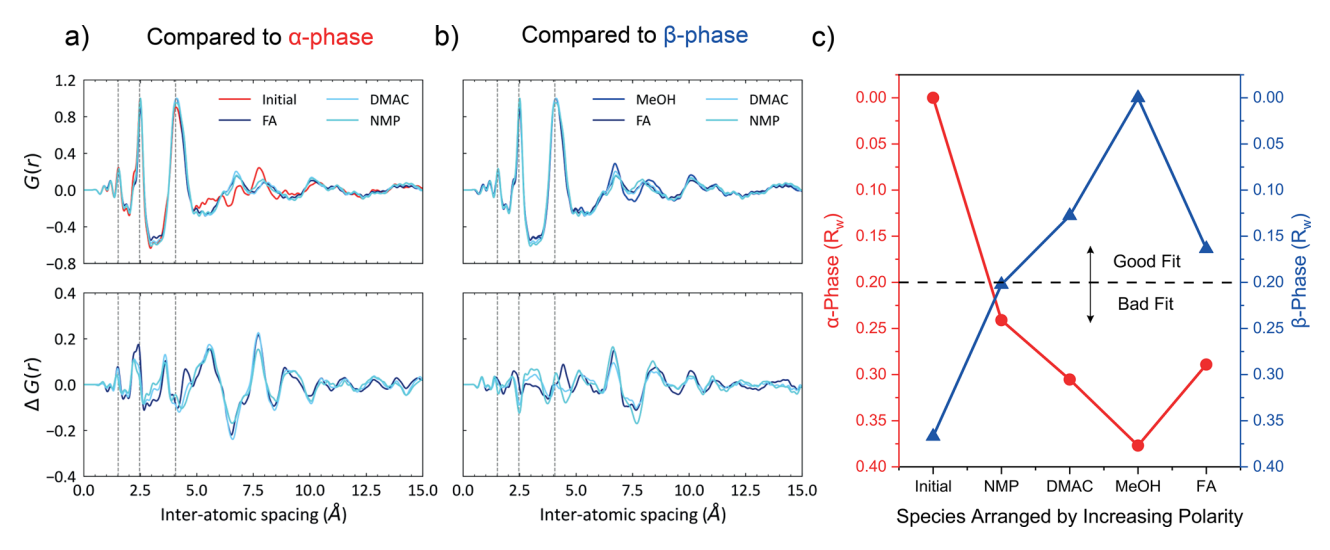


Figure 4. Structural analysis of the β_{367} -phase. Reduced PDF and differential reduced PDF of the β_{367} -phase samples compared to the (a) initial α -phase and (b) MeOH-treated β -phase. Significant deviations are found around 7.5 Å in both cases, but a comparison between the β_{367} -phase and the α -phase reveals greater discrepancies across a range of distances. (c) $R_{\rm w}$ comparison of the amide-treated MSCs with the α -phase and β -phase. The plots indicate a trend toward better fits compared with the MeOH β -phase with rising polarity. All β_{367} -phase samples meet the criteria of a good structural fit to the β -phase standard.

electronic or atomic structure even when ligand binding modes have been modified through small-molecule adsorption. ^{14,15}

While these explanations could explain the change in the electronic structure, they do not explain the reason for the change in the atomic structure. Because isomerization is limited to only small nanocrystals, some size-dependent properties must inhibit larger nanocrystals from accomplishing this change. CdS, CdSe, and InP all have two polymorphs, the zinc blende ($\overline{F43m}$) and wurtzite ($P6_3mc$) crystal structures, and the CdS MSCs in this study tend to be wurtzite-like in the α -phase.² The polar molecules initiating the isomerization have important surface interactions, and the dipole moments of the molecules interact with the surface in a defined way. This orientation leads to a well-defined interaction between the electric field of the molecular dipole moment and the cluster. Because the isomerization inverts after removal of the initiating species, this implies that the MSC is elastically deformed, and when the source of the stress is removed, the MSC returns back to its original shape. Based on this, we hypothesize that the structural changes could arise from a phenomenon resembling the inverse piezoelectric effect. The inverse piezoelectric effect is defined as a third rank tensor relating deformation (strain) to an external electric field. This effect could explain why this phenomenon is not observed in larger nanocrystals as the electric field from the polar molecules is no longer strong enough to produce significant structural changes. This effect has been used to tune the band structure of nanomaterials in piezo-active systems.^{33,34} This effect would explain why isomerization is not observed in the aforementioned InP MSCs (1), which are not ferroelectric due to the inversion symmetry of the cluster and therefore does not have the symmetry to allow for the inverse piezoelectric effect. 14,35 To probe the piezoelectric effect, the MSCs were placed in a cuvette with transparent electrodes with a voltmeter, and the absorbance spectrum was measured. As the potential difference was increased, the MSC absorbance feature redshifted by up to 10 meV (Figure S14). As a control, larger CdS quantum dots (QDs) were also measured using the same setup. The CdS QDs were completely insensitive to the applied potential

difference. Ultimately, the cause of the shift arises from modification of the MSC wave function causing significant changes in the band structure of the inorganic cluster leading to the shift in absorbance. The precise origin of this modification requires further investigation.

Our analysis of the β_{367} -phase PDF G(r) showed pair-length variations depending on the amide used to initiate the isomerization. Each of the amide-treated β_{367} -phase MSCs displayed shifts toward shorter interatomic spacings for the first Cd-S correlation compared to the bulk CdS correlation (Figure S15a-d). While the first Cd-S-Cd correlation of each of the MSC samples did not show any deviation in the peak position compared to the bulk CdS, the higher intensity represented as a shoulder at greater interatomic spacings for all MSC samples indicates a bias toward these larger spacings. From the area under the curve of a G(r) peak, the number of nearest neighbors can be estimated. Bulk CdS has Cd²⁺ cations exclusively in tetrahedral coordination environments.³⁶ The nearest neighbor fraction follows a trend similar to the Rw comparison; MSCs treated with more polar amides generally have higher nearest neighbor fractions (though FA disrupts this trend). Interestingly, the initial MSC has the highest nearest neighbor fraction (Figure S15e). Overall, the CdS MSCs are undercoordinated, which is reasonable when considering the high surface area-to-volume ratio: the underbonded Cd on the surface decreases the nearest neighbor fraction. By quantifying the peak through Gaussian fitting of the first Cd-S correlation peak, the compressive strain of each MSC compared to the bulk was elucidated showing identical strain for all of the treated MSCs other than FA-treated MSCs which showed lower strain values (Figure S15f). Each of the treated MSCs showed strain values lower than those of the initial α -phase MSCs. The FWHM variations between the Gaussian-fitted PDF were negligible indicating that interatomic spacing dispersities are comparable, and the central peak positions of the Gaussian fits accurately represent the average bond lengths (Figure S15g).

Role of Surface Ligand Interactions in the Isomerization Process. To investigate the surface interactions

ı

between the amide species and ligands, FTIR spectroscopy and XPS were employed (Figure 5a,d). Once again, the β_{367} -phase

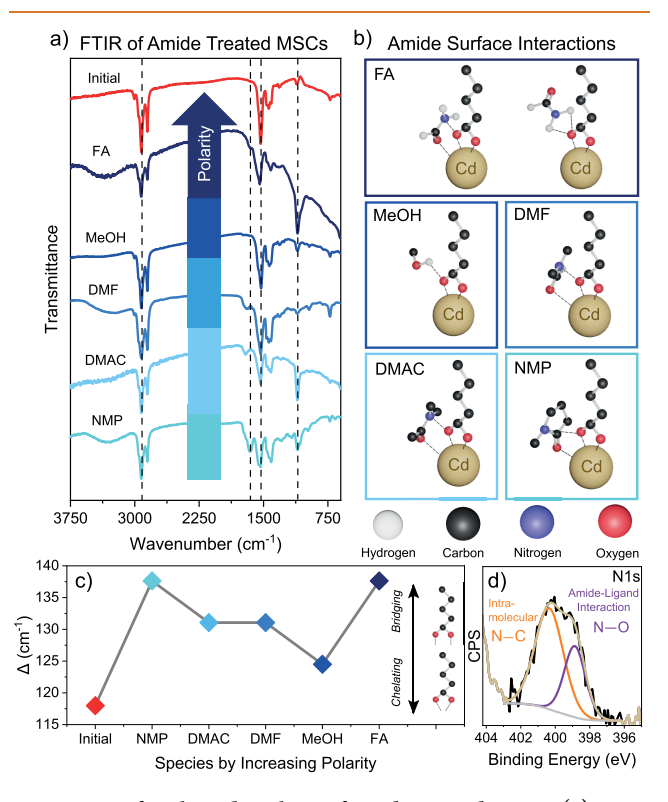


Figure 5. Surface ligand analysis of amide-treated MSCs. (a) FTIR of the amide-treated MSCs compared to initial and MeOH-treated MSCs arranged by increasing polarity. The C-H sp³ stretching, amide-I C=O stretching, asymmetric C=O stretching, and C-O/ C-N stretching peaks are indicated by dashed lines from left-toright. (b) Proposed binding modes of isomerizing species characterized by the L-type interaction of the amide carbonyl with the cadmium cation taking on a planar geometry and the back binding of the amide nitrogen for FA, DMF, DMAC, and NMP. MeOH and FA can form simple hydrogen bonds with the oleate carboxylate group. Electrostatic interactions are indicated by dashed lines. (c) Difference in symmetric and asymmetric carboxylate peaks (Δ) of treated and untreated MSCs shows that all amide species have higher Δ values compared to the initial and MeOH-treated MSCs. Inset illustration indicates the geometry of the bridging and chelating binding modes. (d) Nitrogen 1s XPS spectrum of NMP-treated MSCs showing the intramolecular (N-C) and amide-ligand interaction (N-O) between the amide and carboxylate. The gray line is the background, and the beige line is the envelope fit.

was used so that every amide could be studied in the same atomic phase. In the spectra, there are distinct features around 1100 cm⁻¹, which are more pronounced in the treated samples. These features are assigned as the C–O or C–N stretching modes for each species. The spectra also feature peaks between 1528–1548 and 1712–1660 cm⁻¹ corresponding to the carbonyl stretching modes (C=O) of the amides (amide-I stretching mode) and oleic acid, respectively, which will be explored in detail later in the discussion. Near 3000 cm⁻¹, there are peaks consistent with both sp³ and sp² hybridized C–H stretching modes. The sp² signal is assigned to the *cis* double bond of the oleate ligands. Interestingly, in several of the samples, there is a broad peak centered near 3500 cm⁻¹ that likely belongs to an O–H stretching mode, though in the case

of FA, it may represent poorly resolved N–H stretching modes. The carbonyl stretching frequencies of the amides shifted to higher wavenumbers compared to what is typically observed for primary and tertiary amides (1690–1680 cm⁻¹),³⁷ suggesting that the vibrational modes have been altered by an interaction (Figure 5a).

Each sample displays peaks in the range of 1528–1548 cm⁻¹ that are assigned to the asymmetric carboxylate binding mode and several peaks around 1410 cm⁻¹ that are assigned to the symmetric carboxylate binding mode (Figure 5a). The separation between the asymmetric and symmetric carboxylate FTIR peaks (Δ) gives insight into what type of ligand binding the carboxylates are participating in (chelating, bridging, etc.). Larger separations are characteristic of a bridging binding, while shorter separations correspond to chelating binding. ^{38,39} We do not observe any separations in the monodentate range. The difference in the Δ values for the initial MSCs ($\Delta = 118$ cm⁻¹) and the MeOH-treated MSCs ($\Delta = 124$ cm⁻¹) is consistent with what we have previously reported.² The initial asymmetric peak includes a shoulder centered approximately at 1561 cm⁻¹ and the Δ value of the shoulder is 151 cm⁻¹, which corresponds to the bridging binding mode, indicated by a Δ value exceeding 140 cm⁻¹ (Figure 5c). There is no clear trend on the influence of polarity on Δ ; however, each of the amidetreated MSC FTIR spectra have Δ values larger than the MeOH (Figure 5c). This result indicates that all amides have a greater propensity to reorganize the carboxylate into a bridging binding configuration compared to MeOH and the initial

Our previous report concluded that the ligand-binding mode was biased more toward a chelating geometry through the transformation. However, the shoulder on which this analysis is based, centered at 1580 cm⁻¹, is not present in the FTIR spectrum of the initial α -phase MSCs. Considering that the MSCs were synthesized in the same manner, it is unlikely that this signal arose from a difference between the samples. Rather, we hypothesize that the signal observed at 1580 cm⁻¹ corresponds to an overtone from a prominent peak in the fingerprint region centered at 800 cm⁻¹ (Figure 5a).

Previously, it was hypothesized that methanol initiates the transformation by hydrogen bonding to the carboxylate, which influences the bonding configuration of the carboxylate on the surface and that the change of interaction with the surface initiates the structural transformation.2 The interaction between the amides and the surface ligands appears to be similar in nature to the ligand surface interactions with alcohols as the amides also bias the binding mode of the carboxylate ligands. Unlike methanol, however, it is not immediately apparent what the interaction between the amides and carboxylate ligands is as both primary and tertiary amides facilitate the transformation, and hydrogen bonding cannot account for the interaction in the tertiary amides. The nitrogen atoms in amides tend to be electron poor due to the inductive pull of electron density from the carbonyl group by resonance. DFT calculations show that generally the electron density is highest on the more electronegative atoms (oxygen and nitrogen) (Scheme 1). This distribution of electron density is represented in every amide except FA, which shows a comparatively electron-poor nitrogen atom. This electronpoor nitrogen may explain why FA often deviates from the trends of the other amides. 40 The high electron density on the nitrogen atoms is a result of the electron-donating alkyl groups present on tertiary amides compensating for the strong inductive effect of the carbonyl group. While the nitrogen atoms may still have a significant electron density relative to the oxygen and other nitrogen species (e.g., amines), the nitrogen is still relatively electron poor.

Each amide is multifunctional and can interact with the surface in various ways. The electron-rich sites on the amides allow them to donate electron density to the surface, forming an L-type interaction with the surface cadmium cations. This interaction would reduce the electron density available to the other species (oxygen or nitrogen), allowing it to interact with the bound carboxylate in a similar manner to that of the hydrogen bonding with methanol (Figure 5b). DFT calculations of the HOMO and LUMO of each amide (Figure S16) show that the amides have electrons located on the carbonyl oxygen in the HOMO allowing for L-type interactions as well as empty orbitals in the LUMO allowing for the amide to act as a electrophile. These observations indicate that the amides can form amphoteric interactions with the MSC surface.

The surface interaction is evident through the amide-I frequencies being modulated from what is typically observed for primary and tertiary amides, suggesting that the vibrational modes have been altered by this interaction (Figure 5a). 42-45 When amides bind to metal surfaces, they take on a planar geometry relative to the metal site (Figure 5b).⁴¹ This binding modulates the amide-I stretching mode and shifts it to lower wavenumbers. Alternately, anions can interact with the bound amide pushing the amide-I frequency to higher wavenumbers.⁴⁵ This shift of the amide-I stretching mode toward larger wavenumbers is consistent with what we observe in our FTIR spectra; all but one of the amides have significantly higher amide-I frequencies than the neat amides by 5-85 cm⁻¹. This shift supports the notion of the amides participating in some type of interaction on the surface. This is further substantiated by the nitrogen 1s XPS of NMP-treated MSCs. Only a single nitrogen-containing species was used for surface treatment, yet two nitrogen peaks exist in the spectrum (Figure 5d). This indicates that nitrogen atoms exist in two different chemical environments in this system. 46 Previous studies have shown that pyrrolic nitrogen signals tend to be observed near 400 eV.⁴⁷ Based on this value range, we assign these peaks to the N-C bond within the NMP molecule itself (400.4 eV) and the nitrogen interacting with the surface carboxylate ligand (398.9 eV) as previously discussed.

NMP has a well-defined amide-I peak and a shoulder extending toward larger wavenumbers (Figure 5a). The peak is shifted toward a lower wavenumber compared to the neat amide, while the shoulder is biased toward a slightly higher wavenumber than is typical for this amide. This suggests that NMP can readily bind to the surface of the MSC but cannot effectively interact with the carboxylate compared to the other amides. The poor interaction with the carboxylate is likely a result of the increased steric hindrance from the fivemembered ring containing the amide nitrogen. This supports the XPS observation that the nitrogen signal not interacting with the carboxylate ligands is greater than that of nitrogen signal correlating to the electrostatic interaction (Figure 5d). FA is the only amide that experiences a shift in the opposite direction, suggesting that it may not be binding to the surface of the MSC and likely takes on a geometry more similar to MeOH (Figure 5b, right). When the ligands switch from the chelating binding mode to the bridging binding mode, an additional cadmium cation becomes passivated. A higher

number of passivated cadmium sites stabilize the surface, making this an energetically favorable interaction. The increase in passivated cadmium sites comes at the cost of the relative charge ratio of the ligand to cadmium changing from 1:1 to 1:2. To account for this reduction in charge ratio, the interaction requires two amides for every ligand. DMF and DMAC differ only by a methyl group and have very similar electron distributions, so they influence the binding in a similar manner. FA has two hydrogen atoms capable of hydrogen bonding but also has the most electron-rich carbonyl oxygen and the most electron-poor nitrogen, suggesting that it may be capable of inducing the transformation in a manner similar to both MeOH and the other amides. In contrast, NMP has its nitrogen site in a five-member ring causing significant steric hindrance. We propose that the carbonyl group is responsible for the direct interaction with the surface, acting as an L-type ligand which then pulls electron density away from the electron-poor nitrogen site, enabling them to interact with the carboxylate ligands and initiate the change in the binding mode. This change in surface bonding, in turn, enables the MSC atomic structure to undergo a phase transition.

CONCLUSIONS

Using amides to initiate the α -phase to β -phase isomerization, three intermediate states have been isolated and structurally characterized. The intermediates follow the progression α phase $\rightarrow \beta_{340}/\beta_{350}$ -phase $\rightarrow \beta_{367}$ -phase $\rightarrow \beta$ -phase in an ideal transformation. Not only does the initiating species play a crucial role in product stabilization, but the solvent environment also influences the transformation. Specifically, the polarity of the solvent seems to dictate the stability of the intermediate phases, likely a result of solvent-screening effects. In contrast, the role the polarity of the initiating amide plays is still unclear as the data did not show any clear trends. A more complex theoretical study is required to determine the complex interactions of the system. The β_{350} -phase was shown to have an atomic structure similar to every β -isomer through comparison of G(r). The β_{367} -phase was found to have an atomic structure indistinguishable from that of the β -phase. Despite the similarity of the β -isomer atomic structures, each has a comparatively smaller band gap compared to the β -phase by 325, 439, and 583 meV for the β_{340} -phase, β_{350} -phase, and β_{367} -phase, respectively. This decoupling of the atomic and electronic band structures of the clusters could be attributed to either the nanoscale Stark effect or extreme confinement, but the exact nature remains unclear. The amides display an amphoteric ligand binding motif—interacting both directly with the MSC surface and the carboxylate ligands. These intermediates represent a paradigm shift in the mechanism underpinning the isomerization of CdS MSCs and serve as a fundamental discovery, guiding future discussion of the isomerization of inorganic nanoclusters overall.

METHODS

Materials. The following chemicals were used as received (unless otherwise specified) and were purchased from the following suppliers: Sigma-Aldrich: Cadmium oxide (99.5%, trace metal basis), sulfur powder (\geq 99%), tri-n-octylphsosphine (TOP, 97%), diphenylphsosphine (DPP, 99.9%), DMF (99.8% anhydrous), and calcium hydride (CaH₂, \geq 90%). Aldritch Chemicals: DMAC (99.8% anhydrous) and cadmium sulfide (bulk, 99.995% metal basis). Thermo Scientific: Oleic acid (90% tech. grade). VWR International: Hexane (\geq 97% ACS grade). Oakwood Chemicals: THF (99%). Beantown Chem-

icals: Methanol (MeOH, 99.8%). EMD Chemicals: FA (99.5% ACS grade). Macron Fine Chemicals: Acetone (99.5%, ACS grade). Rohn and Haas: NMP (>90%). The nonanhydrous amides were treated with CaH₂ and filtered with a 0.22 μ m PTFE syringe filter prior to use.

Characterization. All UV—vis absorbance spectra were measured using an Ocean Optics UV—vis DH2000 BAL spectrometer equipped with halogen and deuterium light sources with standard 1 cm quartz cuvettes. All FTIR spectra were measured on a Bruker Vertex V80 V vacuum FTIR system by using a silicon substrate in transmission mode. All XPS data were collected using a Thermo Scientific Nexsa G2 surface analysis system, and all XPS data were fitted using CasaXPS software. PDF data were measured at NSLS-II beamlines 28-ID-1 and 28-ID-2 at Brookhaven National Laboratory.

Synthesis of CdS MSCs. The CdS MSCs were synthesized according to previously published literature with minor modifications.⁴⁸ Cadmium oxide (5 mmol, 0.64 g) and a magnetic stir bar are added to a 50 mL three-necked round-bottom flask and mixed with oleic acid (16 mmol, 5 mL). The flask is connected to a Schlenk line and then placed in a heating mantle and equipped with a thermocouple temperature probe. The mixture is stirred with a magnetic stirrer, degassed starting at room temperature, and slowly heated to 50 $^{\circ}\text{C}$ over 15–20 min. The reaction flask is then flushed with dry N_2 gas and heated to 160 $^{\circ}\text{C}$ for 30 min. The reaction flask is then swirled to remove any cadmium oxide remaining on the sides of the flask. The temperature is then raised to 170 °C and stirred for 1 h. The temperature is then lowered to 110 °C, and the reaction flask is degassed until bubbling ceases (10-15 min). The reaction flask is flushed with N2, and the temperature is lowered to 80 °C. Sulfur powder (2.5 mmol, 0.08 g) and a magnetic stir bar are added to a scintillation vial and loaded into a nitrogen atmosphere glovebox with a 5 mL syringe bearing a hypodermic needle. Trioctylphosphine (2.25 mmol, 1 mL) is added to the sulfur and stirred with a high stirring rate at \sim 80 °C. Once solid sulfur is no longer visible, the vial is cooled and then taken into the syringe and removed from the glovebox. TOPS is injected into the Cd(OA)₂ precursor solution, and the temperature is immediately adjusted to 140 °C. The reaction is allowed to stir for 1 h, then the heating mantle is removed, and the reaction solution is allowed to cool to 70 °C. The reaction solution is then evenly transferred into two 50 mL centrifuge tubes. Acetone (15 mL) is added to each tube and shaken thoroughly. The two tubes are then centrifuged (4500 rpm, 3 min), the supernatant is discarded, and the precipitate is retained. Hexane (25 mL) is added to each tube and vigorously shaken to dissolve the MSCs. Acetone (20 mL) is added to precipitate the MSCs, and the tubes are centrifuged. This wash cycle is repeated two to three times. The precipitate is placed in a vacuum desiccator and dried over a 12-20 h period.

Synthesis of CdS QDs. Cadmium oxide (5.0 mmol, 0.64 g) and a magnetic stir bar are added to a 50 mL three-necked round-bottom flask and mixed with oleic acid (16 mmol, 5 mL). The flask is connected to a Schlenk line then placed in a heating mantle and equipped with a thermocouple temperature probe. The mixture is stirred with a magnetic stirrer and degassed starting at room temperature and slowly heated to 50 °C over 15-20 min. The reaction flask is then flushed with dry N2 gas and heated to 160 °C for 30 min. The reaction flask is then swirled to remove any cadmium oxide remaining on the sides of the flask. The temperature is then raised to 170 $^{\circ}\text{C}$ and stirred for 1 h. The temperature is then lowered to 110 °C, and the reaction flask is degassed until bubbling ceases (10-15 min). The reaction flask is flushed with N_2 , and the temperature is lowered to 80 °C. Sulfur powder (2.5 mmol, 0.08 g) and a magnetic stir bar are added to a scintillation vial and loaded into a nitrogen atmosphere glovebox with a 5 mL syringe bearing a hypodermic needle. Diphenylphosphine (5.7 mmol, 1 mL) is added to the sulfur and stirred at a high stir rate at 90 °C. Once solid sulfur is no longer visible, the vial is cooled, then taken into the syringe, sealed with a septum, and removed from the glovebox. DPPS is injected into the Cd(OA)₂ precursor solution, and the temperature is immediately adjusted to 140 °C. The reaction is continued for 20 h, then the heating mantle is removed, and the reaction solution is rapidly cooled

in an ice bath. The reaction solution is then evenly transferred into two 50 mL centrifuge tubes. Acetone (15 mL) is added to each tube and shaken thoroughly. The two tubes are then centrifuged (4500 rpm, 3 min), the supernatant is discarded, and the precipitate is retained. Hexane (25 mL) is added to each tube, and the tube is vigorously shaken to dissolve the QDs. Acetone (20 mL) is added to precipitate the QDs, and the tubes are centrifuged. This wash cycle is repeated two to three times. The precipitate is placed in a vacuum desiccator and dried over a 12-20 h period.

Isomerization of MSCs. Due to the low vapor pressure and high boiling point of the amides in this study, a vapor approach was not experimentally viable for an in situ study. As such, solution measurements were performed using a series of solvents [hexane, THF, and chloroform (CHCl₃)] to completely dissolve both the MSCs with the aliphatic ligands and amides.

In situ: For initial time studies, 12 mL of MSC solutions (0.3 mg/mL, hexane, THF, CHCl $_3$) were prepared such that the peak height of the peak centered at 324 was approximately 1 absorbance. After a background was taken with the neat solvent, the cuvette was emptied, and 2 mL of the MSC solution was added. After measurement begins, 0.5 mL of the respective amide is added directly to the cuvette. To limit precipitation in the cuvette, a stir bar is used during the measurement. The Arrhenius and Eyring fit of the kinetic data were taken over five temperatures (27.3, 33.2, 37.8, 41.5, and 48.6 $^{\circ}$ C).

Ex situ: For the time studies, 5 mL of MSC solutions (2 mg/mL, hexane) were prepared, and 2 mL of the respective amide was added to the solution and mixed by stirring. 200 μ L aliquots were taken at the indicated time points and added to ~2 mL of hexane for UV–vis measurements. Solutions were stored in air during short time points (i.e., the first 4 h) and were subsequently stored in a N₂ glovebox overnight between longer time points (i.e., t > 12 h).

Isolation of Intermediates. The β_{340} -phase was isolated by preparing 10 mL of 10 mg/mL of α -phase CdS MSCs and then injecting 6 mL of DMF. The solution was stirred at room temperature for 3 h and then precipitated with acetone and dried under vacuum.

The β_{350} -phase was isolated by preparing 10 mL of 10 mg/mL α -phase CdS MSCs and then injecting 1 mL of DMAC. The solution was stirred at room temperature for 15 min and then precipitated with acetone and dried under vacuum.

The β_{367} -phase was isolated by preparing 10 mL MSC solutions (20 mg/mL, THF), and an excess (10 mL) of the respective amide was added to the solution. Each mixture was left to stir under N_2 for 2 weeks. The amide was then removed through precipitation centrifugation and dried under vacuum overnight.

Preparation of FTIR Samples. The solid amide-treated MSCs described previously were redissolved in hexane with a concentration of 2 mg/mL. Then, the resulting solution was drop-cast (approximately 400 μ L) onto a small silicon wafer (200 nm SiO₂ layer) and left to dry in air (<1 min). The sample was then mounted vertically in the FTIR vacuum chamber and measured in transmission using standard instrument procedures.

Preparation of XPS Samples. Sample substrates consisted of an SEM stub covered with conductive double-sided carbon tape. An N-doped silicon wafer shard was then adhered to the conductive tape. The samples were either loaded directly as a powder or drop-cast from solution. Powders were wetted with hexane to improve contact with the substrate. After drying, the samples were then sputter-coated using a Au/Pd argon source for 30 s. Excess coating was ablated using an argon beam.

PDF Data Processing. X-ray total scattering data were collected at the Brookhaven National Lab NSLS-II 28-ID-1 and 28-ID-2 beamlines. Dried samples were preloaded into Kapton capillaries (1 mm outer diameter) and sealed with epoxy. The samples were illuminated with 74.5 keV X-rays with a short sample-to-detector distance. The sample-to-detector distance was calibrated using a Ceria (CeO₂) standard. Each integrated data set is the average of several detector images, collected for 3 min each. The setup enabled collection of total scattering data beyond 33 Å⁻¹; however, due to noise at high-q, the data were typically truncated at 26 Å⁻¹. Then, the

total scattering data were converted to the PDF following reported methods (details in the SI).

ASSOCIATED CONTENT

5 Supporting Information

The Supporting Information is available free of charge at https://pubs.acs.org/doi/10.1021/acsnano.4c08319.

Time-resolved UV—vis spectra of MeOH in chloroform (MP4)

Detailed experimental methods, additional discussion of UV-vis and XPS data, description of kinetic and PDF data processing, description of DFT calculations, additional discussion of strain analysis from PDF data, and supplementary tables and figures (PDF)

AUTHOR INFORMATION

Corresponding Author

Richard D. Robinson — Department of Materials Science and Engineering and Kavli Institute at Cornell for Nanoscale Science, Cornell University, Ithaca, New York 14853, United States; orcid.org/0000-0002-0385-2925; Email: rdr82@cornell.edu

Authors

Reilly P. Lynch – Department of Materials Science and Engineering, Cornell University, Ithaca, New York 14853, United States; orcid.org/0009-0003-3711-8002

Thomas J. Ugras — School of Applied and Engineering Physics, Cornell University, Ithaca, New York 14853, United States; orcid.org/0000-0002-5931-3031

Complete contact information is available at: https://pubs.acs.org/10.1021/acsnano.4c08319

Notes

The authors declare no competing financial interest.

ACKNOWLEDGMENTS

Thank you to the National Science Foundation (NSF, CHE-2003586, CMMI-2120947, DMR-2344586, and DMR-1719875), Kavli Institute at Cornell (KIC), and American Chemical Society Petroleum Research Fund (ACS PRF, PRF # 65116-ND5) for support of this research. This work made use of the Cornell Center for Materials Research Shared Facilities, which are supported through the NSF Materials Research Science and Engineering Centers (MRSEC) program (DMR-1719875). Special thanks to J. De Roo, J. Owen, I. Infante, and D. Milliron for the valuable insight, discussions, and suggestions they shared, to A. Tripp for her assistance in collecting and processing XPS data and to G. Kwon, S. Ghose, M. Kirshenbaum, and S. Rana for their assistance in gathering the PDF data for this study.

REFERENCES

- (1) Dugave, C.; Demange, L. Cis-Trans Isomerization of Organic Molecules and Biomolecules Implications and Applications. *Chem. Rev.* **2003**, *103*, 2475.
- (2) Williamson, C. B.; Nevers, D. R.; Nelson, A.; Hadar, I.; Banin, U.; Hanrath, T.; Robinson, R. D. Chemically reversible isomerization of inorganic clusters. *Science* **2019**, *363* (6428), 731–735.
- (3) Nevers, D. R.; Williamson, C. B.; Hanrath, T.; Robinson, R. D. Surface chemistry of cadmium sulfide magic-sized clusters: a window into ligand-nanoparticle interactions. *Chem. Commun.* **2017**, *53* (19), 2866–2869.

- (4) Zhang, B.; Zhu, T.; Ou, M.; Rowell, N.; Fan, H.; Han, J.; Tan, L.; Dove, M. T.; Ren, Y.; Zuo, X.; Han, S.; Zeng, J.; Yu, K. Thermally-induced reversible structural isomerization in colloidal semiconductor CdS magic-size clusters. *Nat. Commun.* **2018**, *9* (1), 2499.
- (5) Cao, Y.; Malola, S.; Matus, M. F.; Chen, T.; Yao, Q.; Shi, R.; Häkkinen, H.; Xie, J. Reversible isomerization of metal nanoclusters induced by intermolecular interaction. *Chem.* **2021**, *7* (8), 2227–2244.
- (6) Zhang, C.; Wang, Z.; Si, W. D.; Wang, L.; Dou, J. M.; Gao, Z. Y.; Tung, C. H.; Sun, D. Solvent-Induced Isomeric Cu(13) Nanoclusters: Chlorine to Copper Charge Transfer Boosting Molecular Oxygen Activation in Sulfide Selective Oxidation. *ACS Nano* **2022**, *16* (6), 9598–9607.
- (7) Guan, Z. J.; Hu, F.; Li, J. J.; Wen, Z. R.; Lin, Y. M.; Wang, Q. M. Isomerization in Alkynyl-Protected Gold Nanoclusters. *J. Am. Chem. Soc.* **2020**, *142* (6), 2995–3001.
- (8) Chen, Y.; Liu, C.; Tang, Q.; Zeng, C.; Higaki, T.; Das, A.; Jiang, D. E.; Rosi, N. L.; Jin, R. Isomerism in Au28(SR)20 Nanocluster and Stable Structures. J. Am. Chem. Soc. 2016, 138 (5), 1482–1485.
- (9) Chen, X. R.; Yang, L.; Tan, Y. L.; Yu, H.; Ni, C. Y.; Niu, Z.; Lang, J. P. The solvent-induced isomerization of silver thiolate clusters with symmetry transformation. *Chem. Commun.* (*Camb*) **2020**, *56* (25), 3649–3652.
- (10) Wang, Z.; Sun, H. T.; Kurmoo, M.; Liu, Q. Y.; Zhuang, G. L.; Zhao, Q. Q.; Wang, X. P.; Tung, C. H.; Sun, D. Carboxylic acid stimulated silver shell isomerism in a triple core-shell Ag(84) nanocluster. *Chem. Sci.* **2019**, *10* (18), 4862–4867.
- (11) Chen, Z.; Manian, A.; Dong, Y.; Russo, S. P.; Mulvaney, P. Ligand and solvent effects on the absorption spectra of CdS magic-sized clusters. *J. Chem. Phys.* **2023**, *158* (17), 174308.
- (12) Chen, Z.; Ashokan, A.; Russo, S. P.; Mulvaney, P. Temperature Dependence of the CdS Bandgap in the Extreme Confinement Regime. *Nano Lett.* **2023**, 23 (20), 9287–9294.
- (13) Shim, D.; Lee, J.; Kang, J. Multiscale Isomerization of Magic-Sized Inorganic Clusters Chemically Driven by Atomic-Bond Exchanges. *Chem. Mater.* **2022**, 34 (21), 9527–9535.
- (14) Gary, D. C.; Flowers, S. E.; Kaminsky, W.; Petrone, A.; Li, X.; Cossairt, B. M. Single-Crystal and Electronic Structure of a 1.3 nm Indium Phosphide Nanocluster. *J. Am. Chem. Soc.* **2016**, *138* (5), 1510–1513.
- (15) Sandeno, S. F.; Schnitzenbaumer, K. J.; Krajewski, S. M.; Beck, R. A.; Ladd, D. M.; Levine, K. R.; Dayton, D.; Toney, M. F.; Kaminsky, W.; Li, X.; Cossairt, B. M. Ligand Steric Profile Tunes the Reactivity of Indium Phosphide Clusters. *J. Am. Chem. Soc.* **2024**, *146* (5), 3102–3113.
- (16) Uriarte, L. M.; Vitale, R.; Nizinski, S.; Hadjidemetriou, K.; Zala, N.; Lukacs, A.; Greetham, G. M.; Sazanovich, I. V.; Weik, M.; Ruckebusch, C.; Meech, S. R.; Sliwa, M. Structural Information about the trans-to-cis Isomerization Mechanism of the Photoswitchable Fluorescent Protein rsEGFP2 Revealed by Multiscale Infrared Transient Absorption. *J. Phys. Chem. Lett.* 2022, 13 (5), 1194–1202.
- (17) Park, K.; Deutsch, Z.; Li, J. J.; Oron, D.; Weiss, S. Single Molecule Quantum-Confined Stark Effect Measurements of Semiconductor Nanoparticles at Room Temperature. ACS Nano 2012, 6 (11), 10013–10023.
- (18) Grim, J. Q.; Bracker, A. S.; Zalalutdinov, M.; Carter, S. G.; Kozen, A. C.; Kim, M.; Kim, C. S.; Mlack, J. T.; Yakes, M.; Lee, B.; Gammon, D. Scalable in operando strain tuning in nanophotonic waveguides enabling three-quantum-dot superradiance. *Nat. Mater.* **2019**, *18* (9), 963–969.
- (19) Empedocles, S. A.; Bawendi, M. G. Quantum-Confined Stark Effect in Single CdSe Nanocrystallite Quantum Dots. *Science* **1997**, 278, 2114–2117.
- (20) Yu, Q.; Liu, C.-Y. Study of Magic-Size-Cluster Mediated Formation of CdS Nanocrystals: Properties of the Magic-Size Clusters and Mechanism Implication. *J. Phys. Chem. C* **2009**, *113* (29), 12766–12771.
- (21) Kudera, S.; Zanella, M.; Giannini, C.; Rizzo, A.; Li, Y.; Gigli, G.; Cingolani, R.; Ciccarella, G.; Spahl, W.; Parak, W. J.; Manna, L.

- Sequential Growth of Magic-Size CdSe Nanocrystals. Adv. Mater. 2007, 19 (4), 548-552.
- (22) Busatto, S.; Spallacci, C.; Meeldijk, J. D.; Howes, S.; de Mello Donega, C. Room-Temperature Interconversion Between Ultrathin CdTe Magic-Size Nanowires Induced by Ligand Shell Dynamics. *J. Phys. Chem. C Nanomater Interfaces* **2022**, 126 (36), 15280–15297.
- (23) Lancaster, N. L.; Welton, T. Nucleophilicity in Ionic Liquids. 3. Anion Effects on Halide Nucleophilicity in a Series of 1-Butyl-3-methylimidazolium Ionic Liquids. *J. Org. Chem.* **2004**, *69* (18), 5986–5992.
- (24) Martinez-Casado, F. J.; Ramos-Riesco, M.; Rodriguez-Cheda, J. A.; Redondo-Yelamos, M. I.; Garrido, L.; Fernandez-Martinez, A.; Garcia-Barriocanal, J.; da Silva, I.; Duran-Olivencia, M.; Poulain, A. Lead(ii) soaps: crystal structures, polymorphism, and solid and liquid mesophases. *Phys. Chem. Chem. Phys.* **2017**, *19* (26), 17009–17018.
- (25) Terban, M. W.; Billinge, S. J. L. Structural Analysis of Molecular Materials Using the Pair Distribution Function. *Chem. Rev.* **2022**, *122* (1), 1208–1272.
- (26) Christiansen, T. L.; Cooper, S. R.; Jensen, K. M. O. There's no place like real-space: elucidating size-dependent atomic structure of nanomaterials using pair distribution function analysis. *Nanoscale Adv.* **2020**, *2* (6), 2234–2254.
- (27) Thomae, S. L. J.; Prinz, N.; Hartmann, T.; Teck, M.; Correll, S.; Zobel, M. Pushing data quality for laboratory pair distribution function experiments. *Rev. Sci. Instrum.* **2019**, *90*, No. 043905.
- (28) Yang, X.; Masadeh, A. S.; McBride, J. R.; Bozin, E. S.; Rosenthal, S. J.; Billinge, S. J. L. Confirmation of disordered structure of ultrasmall CdSe nanoparticles from X-ray atomic pair distribution function analysis. *Phys. Chem. Chem. Phys.* **2013**, *15* (22), 8480–8486.
- (29) Lambert, J. H. Photometria sive de mensura et gradibus luminis, colorum et umbrae; Augustae Vindelicorum: 1760.
- (30) Anderson, N. C.; Hendricks, M. P.; Choi, J. J.; Owen, J. S. Ligand Exchange and the Stoichiometry of Metal Chalcogenide Nanocrystals: Spectroscopic Observation of Facile Metal-Carboxylate Displacement and Binding. *J. Am. Chem. Soc.* **2013**, *135* (49), 18536–18548.
- (31) Lawrence, K. N.; Dutta, P.; Nagaraju, M.; Teunis, M. B.; Muhoberac, B. B.; Sardar, R. Dual Role of Electron-Accepting Metal-Carboxylate Ligands: Reversible Expansion of Exciton Delocalization and Passivation of Nonradiative Trap-States in Molecule-like CdSe Nanocrystals. *J. Am. Chem. Soc.* **2016**, *138* (39), 12813–12825.
- (32) Cossairt, B. M.; Juhas, P.; Billinge, S. J. L.; Owen, J. S. Tuning the Surface Structure and Optical Properties of CdSe Clusters Using Coordination Chemistry. *J. Phys. Chem. Lett.* **2011**, 2 (24), 3075–3080.
- (33) Zhu, S.; Wu, Y.; Liu, X.; Gong, Z.; Huang, H.; Qin, Q. Tuning the optical band gap of monolayer WSe2 in ferroelectric field-effect transistors. *Ceram. Int.* **2022**, *48* (10), 14231–14236.
- (34) Martín-Sánchez, J.; Trotta, R.; Mariscal, A.; Serna, R.; Piredda, G.; Stroj, S.; Edlinger, J.; Schimpf, C.; Aberl, J.; Lettner, T.; Wildmann, J.; Huang, H.; Yuan, X.; Ziss, D.; Stangl, J.; Rastelli, A. Strain-tuning of the optical properties of semiconductor nanomaterials by integration onto piezoelectric actuators. *Semicond. Sci. Technol.* 2018, 33 (1), No. 013001.
- (35) Smith, M.; Kar-Narayan, S. Piezoelectric polymers: theory, challenges and opportunities. *International Materials Reviews* **2022**, *67* (1), 65–88.
- (36) Wells, A. F. Structural Inorganic Chemistry; Oxford University Press: 1984.
- (37) Pavia, D. A.; Lampman, G. M.; Kriz, G. S.; Vyvyan, J. R. Introduction to Spectroscopy; Cengage Learning: 2013.
- (38) Deacon, G. B.; Phillips, R. J. Relationships Between the Carbon-Oxygen Stretching Frequencies of Carboxylato Complexes and the Type of Carboxylate Coordination. *Coord. Chem. Rev.* **1980**, 33, 227–250.
- (39) Alcock, N. W.; Tracy, V. M.; Waddington, T. C. Acetates and Acetato-complexes. Part 2. Spectroscopic Studies. *J. Chem. Soc., Dalton Trans.* 1976, 2243–2246.

- (40) Reichardt, C.; Welton, T. Solvents and Solvent Effects in Organic Chemistry; Wiley VCH: 2011.
- (41) Clement, O.; Rapko, B. M.; Hay, B. P. Structural aspects of metal-amide complexes. *Coord. Chem. Rev.* 1998, 170 (1), 203-243.
- (42) Cai, M. F.; Smart, R. B. Quantitative analysis of N-methyl-2-pyrrolidinone in coal extracts by TGA-FTIR. *Energy Fuels* **1993**, 7 (1), 52–56.
- (43) Sangeetha, T.; Naganandhini, S. P.; Shanmugam, R.; Arivazhagan, G. FTIR Spectral Signatures of Formamide + Propionic/Acetic Acid Solutions. *J. Solution Chem.* **2022**, *51* (2), 167–189.
- (44) Verbovy, D. M.; Smagala, T. G.; Brynda, M. A.; Fawcett, W. R. A FTIR study of ion-solvent interactions in N,N-dimethylacetamide. *J. Mol. Liq.* **2006**, *129* (1–2), 13–17.
- (45) Ohashi, K.; Takeshita, H. Infrared spectroscopic and computational studies of Co(ClO4)2 dissolved in N,N-dimethylformamide (DMF). Vibrations of DMF influenced by Co2+ or ClO4- or both. Spectrochim. Acta, Part A 2021, 248, No. 119289.
- (46) Bagus, P. S.; Nelin, C. J.; Brundle, C. R. Chemical significance of x-ray photoelectron spectroscopy binding energy shifts: A Perspective. *J. Vac. Sci. Technol., A* **2023**, *41* (6), No. 068501.
- (47) Qu, D.; Sun, Z.; Zheng, M.; Li, J.; Zhang, Y.; Zhang, G.; Zhao, H.; Liu, X.; Xie, Z. Three Colors Emission from S,N Co-doped Graphene Quantum Dots for Visible Light H2 Production and Bioimaging. Advanced Optical Materials 2015, 3 (3), 360–367.
- (48) Nevers, D. R.; Williamson, C. B.; Savitzky, B. H.; Hadar, I.; Banin, U.; Kourkoutis, L. F.; Hanrath, T.; Robinson, R. D. Mesophase Formation Stabilizes High-Purity Magic-Sized Clusters. *J. Am. Chem. Soc.* 2018, 140 (10), 3652–3662.